Revision 1

Regular article

Thalliomelane, $TlMn^{4+}_{7.5}Cu^{2+}_{0.5}O_{16}$, a new member of the coronadite group from the preglacial oxidation zone at Zalas, southern Poland

Thalliomelane, $TlMn^{4+}_{7.5}Cu^{2+}_{0.5}O_{16}$, a new member of coronadite group from Zalas, southern Poland

BOŻENA GOŁĘBIOWSKA[1]*, ADAM PIECZKA[1], MACIEJ ZUBKO[2, 3], ANDREAS VOEGELIN[4], JÖRG GÖTTLICHER[5], GRZEGORZ RZEPA[1]

[1] Department of Mineralogy, Petrography and Geochemistry, AGH University of Science and Technology, Mickiewicza 30, 30-059 Kraków, Poland

[2] University of Silesia in Katowice, Institute of Materials Engineering, 41-500 Chorzów, 75 Pułku Piechoty 1a, Poland

[3] University of Hradec Králové, Faculty of Science, Department of Physics, Rokitanského 62, 500 03, Hradec Králové, Czech Republic

[4] Eawag, Swiss Federal Institute of Aquatic Science and Technology, Department of Water Resources and Drinking Water, Überlandstrasse 133, CH-8600 Dübendorf, Switzerland

[5] Karlsruhe Institute of Technology, Institute for Photon Science and Synchrotron Radiation, KIT Campus North, Hermann-von-Helmholtz-Platz 1, D-76344 Eggenstein-Leopoldshafen, Germany

**corresponding author*: goleb@agh.edu.pl

ABSTRACT

Thalliomelane, a new member of the coronadite group (hollandite supergroup), was discovered at Zalas near Cracow in southern Poland (the southern margin of the Cracow–Silesia Monocline) in relics of a preglacial supergene mineralization disseminated in a fault breccia in Middle Jurassic sandy limestone. The mineralization formed at the expense of a sulfide assemblage, which was most likely the source of thallium, related to rejuvenation of Early-Paleozoic fault zones in the Sava phase of the Alpine orogeny. Thalliomelane occurs rarely, and exclusively in the form of fibrous and highly porous tiny aggregates < 50 μm in size that fill small fractures and voids in the sandy limestone host rock. Microprobe analyses based on 16 O and 8 octahedral cations per formula unit resulted in the mean empirical formula $(Tl_{0.77(10)}Ba_{0.21(3)}K_{0.03(1)}Na_{0.01(0)}Pb_{0.01(0)})_{\Sigma 1.03(7)}(Mn^{4+}_{7.15(11)}Cu^{2+}_{0.63(4)}Co^{2+}_{0.08(3)}Fe^{3+}_{0.06(3)}Ni^{2+}_{0.03(1)}Si_{0.03(2)}Mg_{0.01(1)})_{\Sigma 8}[O_{15.67(24)}(OH)_{0.33(24)}]$, corresponding to the formula $Tl(Mn^{4+}_{7.5}Cu^{2+}_{0.5})O_{16}$ for the thalliomelane end-member. The mineral crystallizes in the tetragonal system, space group $I4/m$, and has unit-cell parameters $a = 9.8664(12)$, $c = 2.8721(4)$ Å, $V = 279.59(8)$ Å^3, $Z = 1$. The crystal structure of thalliomelane, measured with 3D electron-diffraction, was refined to an R_1 index of 23.74%. Thalliomelane has the hollandite-type structure. The Mn^{4+} cations, substituted by Cu^{2+} at an amount of ~0.5 apfu, are octahedrally coordinated by oxygen atoms. Four double chains of edge-sharing (Mn,Cu)-O octahedra share corners with each other to form tunnels along the [001] direction. Tl^+ cations are located in the tunnels, occupying partially the origin and centre of the unit cell. The formation of thalliomelane was most probably connected to the weathering of a sulfide mineral assemblage under semi-arid to arid climate. It resulted in the release of Tl and other components of the mineralization into water under the influence of Cl-,

Br- and I-bearing brines and pore waters from the Carpathian flysch or from sediments of the Carpathian foredeep mobilized by compaction during the Sava phase. Via the interaction of these waters, the primary ores altered mainly into goethite, cuprite, malachite, Mn oxides of the coronadite type, with subordinate Cu sulfates, Pb arsenates, Bi oxy-chlorides, and traces of iodargyrite. This assemblage indicates oxidation at progressively increasing pH of ~8–10 and Eh of the order of +0.4–0.5 V. In this setting, thalliomelane could have formed from a cryptomelane-type Mn oxide in contact with Tl-bearing aqueous solutions through Tl-for-K exchange over time.

Keywords: thalliomelane, thallium, Mn oxide, hollandite supergroup, coronadite group, chemical composition, crystal structure, supergene Tl mineral.

INTRODUCTION

The hollandite supergroup contains a number of manganese (Mn) and titanium (Ti) oxides, often referred to as tunnel oxides, which are divided into two groups: the coronadite group and priderite group, depending on the dominant tetravalent cation (Mn^{4+} and Ti^{4+}, respectively) in the octahedral sites (Biagioni et al. 2013). The general formula of these minerals may be written as either $A^{2+}[M^{4+}_{6}M^{3+}_{2}]O_{16}$ or $A^{1+}[M^{4+}_{7}M^{3+}]O_{16}$, or more rarely as $A^{2+}[M^{4+}_{7}M^{2+}]O_{16}$ or $A^{1+}[M^{4+}_{7.5}M^{2+}_{0.5}]O_{16}$, where $A^{1+,2+}$ = large monovalent or divalent cations: Na, K, Tl (in thalliomelane), Pb, Ba, Sr; M^{2+} = Fe and Cu (in thalliomelane); M^{3+} = Mn, Fe, Cr, V; and M^{4+} = Mn and Ti (Biagioni et al. 2013). Thalliomelane, ideally $Tl(Mn^{4+}_{7.5}Cu^{2+}_{0.5})O_{16}$, is the fifth known supergene Tl mineral species besides avicennite, Tl_2O_3 (Karpova et al. 1958), dorallcharite, $(Tl,K)Fe^{3+}_{3}(SO_4)_2(OH)_6$ (Balić-Žunić et al. 1994), lanmuchangite, $TlAl(SO_4)_2 \cdot 12H_2O$ (Daiyan et al. 2003), and thalliumpharmacosiderite, $TlFe_4(AsO_4)_3(OH)_4 \cdot 4H_2O$ (Rumsey et al. 2014). Four

other Tl minerals related to oxygen: chrysothallite, $K_6Cu_6Tl^{3+}Cl_{17}(OH)_4 \cdot H_2O$ (Pekov et al. 2013, 2015), markhininite, $TlBi(SO_4)_2$ (Filatov et al. 2013; Siidra et al. 2014a), karpovite, $Tl_2VO(SO_4)_2(H_2O)$ (Vergasova et al. 2013; Siidra et al. 2014b), and evdokimovite, $Tl_4(VO)_3(SO_4)_5(H_2O)_5$ (Siidra et al. 2013, 2014c) are products of the crystallization of fumarole gas; the remaining from above 100 Tl mineral species known so far are mainly sulfides, arseno- or antimono-sulfides related to hydrothermal activity. Thalliomelane and its name were approved by the Commission on New Minerals, Nomenclature and Classification of the International Mineralogical Association (IMA CNMNC), proposal 2019-055 (Gołębiowska et al. 2020). By analogy to cryptomelane and strontiomelane, two other minerals of the coronadite group, the name of the mineral indicates the main constituent (Tl) and the affinity to dark-colored manganese oxides. The holotype thalliomelane is deposited in the collection of the Mineralogical Museum of the University of Wrocław (Faculty of Earth Sciences and Environmental Management, Institute of Geological Sciences, Mineralogical Museum, 50-205 Wrocław, Cybulskiego 30, Poland), with the catalogue number MMWr IV8025.

OCCURRENCE

Thalliomelane was found in a fault breccia encrusted with supergene Cu minerals and iodargyrite, exposed in 2005 in the active rhyodacite quarry at the Zalas village near Cracow, southern Poland (latitude 50.08426, longitude 19.64441; Gołębiowska et al. 2010, 2015). The village is located approximately 5 km south of Krzeszowice (approx. 20 km west of Cracow), in the southern margin of the Cracow–Silesia Monocline (CSM), which was formed during the Laramide orogeny from Triassic, Jurassic and Cretaceous deposits. The southern part of the monocline is arranged as a system of horsts and grabens, resulting from the northward overthrusting of Carpathian flysch nappes in Paleogene during the Alpine orogeny. The basement

of the monocline is built of Wend to Carboniferous sediments with numerous sequences of Upper Carboniferous and Permian volcanic rocks occasionally exposed at the surface. Zalas is known, first of all, for an abundant assemblage of Middle and Upper Jurassic fossils, occurring within the cover of a Permian rhyodacite laccolith, 281(4) Ma old (Nawrocki et al. 2005), which is exploited in a large quarry. In 2005, quarrying operations exposed a small fault zone cutting the Middle Jurassic sandy limestone occurring in the rhyodacite capstone, with a fault breccia locally encrusted by subordinate hydrothermal and supergene mineralization. The mineralization was composed mainly of Fe and Mn oxides and hydroxides and malachite, with rare, minute relics of sulfides represented by chalcopyrite, covellite, Ag-enriched chalcocite, galena, pyrite, marcasite, and also native bismuth, associated with cuprite, mottramite, Cu sulfates, a Pb-Al arsenate, Bi oxy-chlorides and iodargyrite. The primary sulfide mineralization was related to rejuvenation of Early-Paleozoic fault zones in the Sava phase od the Alpine orogeny, cutting the ore-mineralized basement of the CSM, which later subjected intensive weathering under semi-arid and arid climate between the Oligocene and Middle Miocene (Gołębiowska et al. 2010, 2015).

PHYSICAL PROPERTIES

Thalliomelane was found in only one fragment of the encrusted breccia. It occurs outside the main mass of supergene encrustations, in the form of tiny aggregates < 50 μm in size, filling small fractures and voids in the host sandy limestone. The texture of the fillings is fibrous (maximum thickness of the fibers is only ~1–2 μm) and highly porous (Fig. 1). In spite of the nano-sized texture of the oxide, its fibers seem to be homogeneous. Streak, luster, hardness, cleavage, tenacity and optical properties were not observed due to the fibrous texture of the crystallites. Density was not measured for the same reason; the density calculated on the basis of empirical composition of the type thalliomelane and its unit-cell volume is 5.285 g/cm^3, and

120 5.370 g/cm^3 for the ideal composition. Using the empirical formula and calculated density, the
121 mean refractive index obtained from Gladstone-Dale relation (Mandarino 1979, 1981) is 2.61,
122 and ideal thalliomelane should have a mean refractive index of 2.68.
123

124 ## MICRO-FOCUSED X-RAY FLUORESCENCE SPECTROMETRY (μ-XRF)
125 ## AND X-RAY ABSORPTION SPECTROSCOPY (μ-XAS)

126 A petrographic thin section containing a Tl-rich Mn-particle embedded in $CaCO_3$ matrix was
127 analyzed by μ-XRF (Tornado M4, Bruker Nano GmbH; Ag X-ray tube; 25-μm beam). Element
128 distribution maps around a selected particle showed a clear correlation between Mn, Tl, Cu and
129 Ba in the Mn oxide particle and an inverse correlation with Ca (Fig. 2). A semi-quantitative
130 fundamental parameter analysis of the μ-XRF spectrum integrated over the central part of the Mn
131 oxide particle returned molar ratios of 0.06 Tl/Mn, 0.10 Cu/Mn and 0.03 Ba/Mn. These values
132 deviate somewhat from the ratios determined for thalliomelane based on electron probe micro-
133 analysis (EPMA) on individual mineral grains (0.11 Tl/Mn, 0.09 Cu/Mn, 0.03 Ba/Mn; see the
134 section *Chemical composition*). This deviation may be due to the semi-quantitative nature of the
135 μ-XRF quantification and the potential analyzes of multiple Mn oxides within the analyzed zone
136 (area of ~45 × 75 μm^2 with ~25-μm X-ray beam). On the other hand, the desktop μ-XRF analysis
137 is made on a selected (Tl,Mn)-bearing particle, whereas EPMA analysis with results presented in
138 Table 1 is an average of 14 spot analyzes on different particles with the highest, but varying
139 contents of Tl_2O.
140 μ-XAS data at the Tl L_{III}-edge and the Cu and Mn *K*-edges of the Mn-rich particle were
141 recorded at the SUL-X beamline of the Synchrotron Radiation Source of the Karlsruhe Institute
142 of Technology, using a microfocused X-ray beam with a size of ~40 × 40 μm. The spectra were
143 recorded in fluorescence mode with a 7-element Si(Li) solid state detector. Comparison of the Tl

144 L_{III}-edge X-ray absorption near-edge structure (XANES) spectrum of the sample to the spectra of
145 Tl_2O_3 and hydrated Tl^+ as proxies for Tl^{3+} and Tl^+ clearly showed that Tl in the Mn-rich particle
146 is monovalent (Fig. 3a). Comparison of the Cu *K*-edge XANES spectrum to reference spectra of
147 Cu^+ and Cu^{2+} indicated that Cu was mainly present as Cu^{2+} (data not shown). The Mn *K*-edge
148 extended X-ray absorption fine structure (EXAFS) spectrum of the Mn-rich particle relatively
149 closely matched the reference spectrum of hollandite, and was clearly different from the
150 reference spectra of triclinic birnessite and todorokite (Fig. 3b). This similarity pointed to a
151 similar local Mn coordination in the Mn-rich particle as in the hollandite reference, in line with
152 the identification based on 3D electron diffraction data of the Tl-rich Mn-oxide mineral as a
153 member of the coronadite group (see the section *Crystal structure*).
154

155 ## CHEMICAL COMPOSITION

156 Electron probe micro-analyses of thalliomelane were performed at the Inter-Institute Analytical
157 Complex for Minerals and Synthetic Substances at the University of Warsaw, Poland. The
158 Cameca SX 100 electron microprobe was operated in wavelength-dispersive (WDS) mode with
159 an accelerating voltage of 15 kV, a beam current of 20 nA, peak count-time of 20 s, background
160 time of 10 s, and a beam diameter of 0 (focused) or 1 μm. Standards, analytical lines, diffracting
161 crystals and mean detection limits (wt% element) were as follows: albite – Na (*K*α, TAP, 0.02),
162 Al (*K*α, TAP, 0.01) and Si (*K*α, TAP, 0.02), forsterite – Mg (*K*α, TAP, 0.01), orthoclase – K (*K*α,
163 PET, 0.01), wollastonite – Ca (*K*α, PET, 0.02), rhodonite – Mn (*K*α, LIF, 0.05), hematite – Fe
164 (*K*α, LIF, 0.05), cobaltite – Co (*K*α, LIF, 0.06), NiO – Ni (*K*α, LIF, 0.04), cuprite – Cu (*K*α, LIF,
165 0.04), sphalerite – Zn (*K*α, LIF, 0.06), $SrSO_4$ – Sr (*L*α, PET, 0.03), baryte – Ba (*L*α, PET, 0.05)
166 and S (*K*α, PET, 0.03), TlBrJ – Tl (*M*α, PET, 0.04) and galena – Pb (*M*α, PET, 0.03). The raw
167 data were reduced with the PAP routine of Pouchou and Pichoir (1991) using the CAMECA

software for the electron microprobe. From the 14 spot analyzes with the highest Tl_2O contents (> 15 wt%; Gołębiowska et al. 2015), the average empirical composition of thalliomelane was derived (Table 1). In our opinion, this procedure ensures best comparability of the EPMA results with the composition of the mineral in the thin film that was prepared by Focused Ion Beam (FIB) from a Tl-rich area [brightest in back-scattered-electron (BSE) images], and that was used for 3D electron-diffraction structure refinement. In the formula calculation Fe was assumed to be trivalent, and Co, Ni and Cu divalent based on the respective pH–Eh diagrams of Takeno (2005). For the same reason, and based on the Tl L_{III}-edge XANES spectrum of the (Tl,Mn)-oxide which showed Tl to be mainly Tl(I), the valency +1 was assigned to Tl. Calcium determined by EPMA was excluded from the formula calculation, because it correlates negatively with all main components of the oxide. It was considered as admixture of $CaCO_3$ from the host limestone. Therefore, CaO is mentioned in a note under Table 1 only as microprobe-analyzed component, but not as constituent of the (Tl,Mn)-oxide. Accordingly, a corresponding amount of CO_2, in an atomic proportion equal to Ca, was included as an additional component in the analytical spots that could not be analyzed by EPMA. Due to scarcity of thalliomelane in the available sample and its microfibrolitic texture, IR spectroscopic confirmation of the presence of H_2O was not possible. Tests to record the Raman spectrum of thalliomelane on its fibers were not successful because the mineral was not stable under the laser beam. Therefore, the empirical formula was calculated, considering the trace presence of H_2O according to the coronadite-group stoichiometry, on the basis of 16 (O, OH) anions and 8 octahedral M cations per formula unit (Biagioni et al. 2013). The contents of elements along with analytical accuracies (sd; element standard deviation) are presented in Table 1, and the resulting empirical formula is $(Tl_{0.77(10)}Ba_{0.21(3)}K_{0.03(1)}Na_{0.01(0)}Pb_{0.01(0)})_{\Sigma 1.03(7)}(Mn^{4+}_{7.15(11)}Cu^{2+}_{0.63(4)}Co^{2+}_{0.08(3)}Fe^{3+}_{0.06(3)}Ni^{2+}_{0.03(1)}Si_{0.03(2)}Mg_{0.01(1)})_{\Sigma 8}[O_{15.67(24)}(OH)_{0.33(24)}]$, which leads to the simplified formula of the thalliomelane

This is the peer-reviewed, final accepted version for American Mineralogist, published by the Mineralogical Society of America.
The published version is subject to change. Cite as Authors (Year) Title. American Mineralogist, in press.
DOI: https://doi.org/10.2138/am-2021-7577. http://www.minsocam.org/

mineral, $[(Tl,K),Ba^{2+}][(Mn,Si)^{4+},(Cu,Co,Ni)^{2+}]_8(O,OH)_{16}$, and the respective end-member formula, $Tl(Mn^{4+}_{7.5}Cu^{2+}_{0.5})O_{16}$. This end-member formula corresponds to (in wt%) 23.49 Tl_2O, 72.11 MnO_2, and 4.40 CuO (sum 100).

In the classification of Strunz (Strunz and Nickel 2001) thalliomelane occurs in class "4: OXIDES (Hydroxides, V[5,6] vanadates, arsenites, antimonites, bismuthites, sulfites, selenites, tellurites, iodates); D: Metal:Oxygen = 1:2 and similar; K : With large (+- medium-sized) cations; tunnel structures". In the classification of Dana (Gaines et al. 1997), it belongs to class "7 : MULTIPLE OXIDES; 9 : AB_8X_{16}".

CRYSTAL STRUCTURE

Data collection and refinement

Single-crystal X-ray diffraction studies could not be carried out because of the small cross section of the fibrous crystals of only 1–2 μm^2 and the very small amount of the available (Tl,Mn)-bearing oxide. Therefore, the structural studies of thalliomelane were made applying 3D electron-diffraction using transmission electron microscopy (TEM). The studies were performed using a JEOL JEM 3010 instrument with 300 kV accelerating voltage, equipped with 2k × 2k OriusTM 833 SC200D Gatan CCD camera and Nanomegas Digistar electron beam precession attachment. For TEM analysis, a thin film from a Tl-rich portion of thalliomelane was prepared by Focused Ion Beam (FIB) method using FEI Quanta 3D 200i scanning electron microscope (SEM) equipped with Ga ion gun. The TEM measurements aimed for crystal structure solution were performed using Precession Electron Diffraction method (Vincent and Midgley 1994; Gjönnes 1997; Kolb et al. 2007). The precession electron diffraction patterns were collected from 57° angular range with 1° step and 1° precession angle. The acquisition time was 1 s per one electron diffraction pattern. The possible measurement range was limited by the fact that the studied

crystal was partly shadowed by the specimen holder. The unit-cell determination and data reduction was performed using PETS software (Palatinus et al. 2019) and further data analysis was performed using the software code Jana2006 (Petříček et al. 2014). After careful analysis of the symmetry, two possible space groups were chosen: *I*2/*m* or *I*4/*m*. The first attempt to solve the crystal structure was undertaken in the higher symmetry space group. Structure solution procedure was performed with the charge flipping method using the SuperFlip software implemented in Jana2006. The initial model was refined and missing atoms were found using Fourier maps analysis. Final refinement of the obtained model was performed using SHELXL software package (Sheldrick 2015) and the refinement converged at a *R*1 value of 23.74%. X-ray powder diffraction data were not collected for the reasons presented above. However, TEM diffraction pattern (Table 2) were calculated for all observed reflections of the electron beam on the basis of the refined structural parameters.

Structure description

The details regarding the refined model of the thalliomelane structure (atom positions, selected interatomic distances) are listed in the CIF file attached as Supplemental Material. Thalliomelane has tetragonal symmetry with the space group *I*4/*m.* Unit-cell parameters are a = 9.8664(12), c = 2.8721(4) Å, and V = 279.59(8) Å^3 for Z = 1. The resulting structural model of thalliomelane is similar to the hollandite structure. Divalent cations, represented in thalliomelane dominantly by Cu^{2+} at an amount of ~0.5 apfu, are octahedrally coordinated by O. Four double chains of edge-sharing (Mn^{4+},Cu^{2+})-O octahedra share corners with each other to form tunnels along the [001] direction (Fig. 4a-d). Tl^{+} cations are located in the tunnels along the [001] direction. They occupy the origin and centre of the unit cell. The refined < *M*1=(Mn,Cu)–O > bond length of 1.93(4) Å corresponds well to the bond length of 1.91 Å calculated on the basis of Shannon's (1976) ionic radii of the complex M1 cation and O^{2-}. Each Tl cation has eight neighboring O atoms creating

cuboid-like coordination. The refined Tl–Tl distance (along the c-axis) of 2.8721(4) Å is shorter than the calculated ^{VIII}A–^{VIII}A distance (2 · 1.546 Å = 3.09 Å) and the ideal $^{VIII}Tl^{+}$–$^{VIII}Tl^{+}$ distance (2 · 1.59 Å = 3.18 Å). As a result, the tunnel sites are occupied in the studied oxide only at 50%. The Tl atomic displacement ellipsoids are elongated along the [001] direction, indicating slight disorder of the oxygen anion positions in the tunnels. The *a:c* ratio of thalliomelane calculated from unit-cell parameters, 1 : 0.291, is comparable to the values of analogous ratio in ferricoronadite 1 : 0.293, and manjiroite 1 : 0.289, two other members of the coronadite group with tetragonal symmetry (Table 3).

GENETIC IMPLICATIONS

The occurrence of thalliomelane, $TlMn^{4+}_{7.5}Cu^{2+}_{0.5}O_{16}$, at Zalas, in close proximity to polymetallic encrustations with cuprite, malachite and iodargyrite, suggests that Tl from a source in the CSM basement was transported along rejuvenated fault zones cutting the basement and deposited together with sulfide ores, which subsequently intensively weathered with participation of saline fluids in semi-arid to arid climate. Weathering conditions of the primary ores and formation of the supergene assemblage with thalliomelane may be explained on the basis of thermodynamic stabilities of Cu and Ag minerals and dissolved Cu, Ag, S, Cl, CO_2 and I species at 25 °C and p = 1 bar (Reich et al. 2009), supplemented by stabilities of Tl and Mn species in hydrous environments using the respective pH–Eh diagrams of Brookins (1988), Vink (1993) and Takeno (2005).

The diagrams for thallium by Vink (1993) and Takeno (2005) suggest that over the entire range of H_2O stability, Tl in water should occur primarily as monovalent Tl^{+} cation. Although Tl^{+} is considered to be the dominant Tl species, Tl^{3+} may occur under certain conditions, e.g. for example at a very high Tl concentration, or due to stabilization in layered birnessite-type oxides

(e.g. Bidoglio et al. 1993; Peacock and Moon 2012; Voegelin et al. 2015, Cruz-Hernández et al. 2019, 2020; Wick et al. 2019). Brookins (1988) considered that under oxidizing conditions, thallium oxides: Tl_2O, Tl_2O_3 and Tl_2O_4 dominate the Eh–pH space in order with increasing Eh, and only under strongly acidic oxidizing conditions Tl^{3+} appears. However, the Tl L_{III}-edge XANES spectrum of thalliomelane clearly shows that Tl is dominantly, if not entirely, monovalent Tl^{+}. Moreover, we did not find Tl, even in traces, in asbolane that associated relicts of the primary ores, and thalliomelane was found only in peripheral zone of the supergene encrustations. This location is easily explained by the high solubility of TlOH of ~350 g/l at 18°C (Lin and Nriagu 1998) in contrast to the low solubility of $Tl(OH)_3$, ~0.8 μmol/l = ~0.2 mg/l (Savenko 2000). Hence, a rapid precipitation is unlikely, and Tl could migrate to areas more distant from the primary ores and other supergene components. The Eh–pH stability diagram of Reich et al. (2009) along with Tl and Mn data of Takeno (2005) indicate the most probable pH and Eh conditions during oxidation of the Zalas primary sulfides (Fig. 5). The sulfides [pyrite, marcasite, galena, chalcopyrite, Ag-bearing chalcocite, covellite, acanthite or (Ag,As)- or (Ag,Bi)-sulfosalts] formed most likely from hydrothermal solutions enriched in H_2S during rejuvenation of Paleozoic ore mineralization in the Sava phase of the Alpine orogeny. Then, the mineralization underwent oxidation in an arid climate probably in the period between Late Oligocene to Mid Miocene (Gołębiowska et al. 2010). The oxidation typically formed, first, water dissolved species Cu^{+} and Cu^{2+}, SO_4^{2-}, Fe^{2+} and Fe^{3+} with traces of Mn^{2+} and Tl^{+}, and next, most likely, Cu and Fe sulfates, cuprite and goethite; all found in the Zalas weathering suite. Interaction with the host Upper Jurassic sandy limestone resulted in increasing pH and crystallization of malachite. The rejuvenated fold zones could also have been migration paths for Cl-, Br- and I-bearing brines and pore waters from the Carpathian flysch or from sediments of the Carpathian foredeep mobilized by compaction during the Sava phase (Gołębiowska et al. 2010).

Passing up through the mineralization, the brines could leach and transport away trace amounts of metals, most probably as halide and sulfate complexes. Another possible scenario may correspond to oxidation in arid periods with a deep-seated water table connected with the evaporation of salt lakes or an Neogene inland sea that delivered halide and sulfate ions to the groundwater oxidation system in the Early–Middle Miocene. The fluid chemistry is well documented by the presence of secondary Cu sulfates, Bi oxychlorides and iodargyrite in the supergene products. In combination, these phases point to a high degree of evaporation and salination during the oxidation of the primary ores, and, by the co-presence of malachite and iodargyrite, an increased pH of ~8–10 (Gołębiowska et al. 2010) and Eh of the order of +0.3–0.4 V. Manganese could be mobilized from admixtures during oxidation of primary sulfides, e.g., from chalcopyrite and sphalerite. A further Eh increase may then have led to the immobilization of Mn by the precipitation of Mn^{4+} oxides. Primary MnO_2 precipitates tend to be of nanocrystalline nature. Because of their high specific surface area and negative surface charge, they exhibit a very high sorption capacity towards many trace cations such as Pb^{2+}, Cu^{2+}, Co^{2+}, Zn^{2+}, Ni^{2+}, Ba^{2+}, or Sr^{2+}, e.g., Post et al. (1982), Post (1999). The selective sorption of Tl onto Mn oxide in marine ferromanganese nodules usually results in Tl loadings of the order of 100 mg/kg (Peacock and Moon 2012), with higher Tl contents up to 675 mg/kg recorded in highly-loaded deposits (Haynes et al. 1985; Koschinsky and Hein 2003; Hein et al. 2012). Data on Tl concentrations in individual Mn oxides are scarce. Crittenden et al. (1962) noted up to 3700 mg Tl/kg in hollandite-cryptomelane from the Apache Mine in Arizona. Other examples of Tl-bearing Mn oxides include a psilomelane from Central Kazakhstan (up to 1000 mg Tl/kg; Voskresenskaya and Soboleva 1961), cryptomelane from natural black pigments (up to 2000 mg Tl/kg; Jezequel et al. 2011), and hollandite from the Black Canyon shaft, New Mexico, U.S.A. (up to 5000 mg Tl/kg; Hewett 1968), and this is probably the highest Tl content found in any Mn

oxide to date except that at Zalas. Similarly high level of Tl enrichment in the MnO_2 oxides from Zalas was noted in Cu-bearing coronadite (0.36–0.51 Tl_2O wt%, i.e., ~3560–4900 mg Tl/kg; Gołębiowska et al. 2015). The variations in Tl loadings can be related to differences in Mn oxide structure and Tl uptake capacity, as well as to differences in dissolved Tl concentrations during Tl uptake.

In Mn oxides from Zalas, high contents of Tl, Cu, Co, Ni and Pb suggest their direct relation with the primary ore assemblage. The oxides are mainly represented by coronadite-group minerals, including thalliomelane. Thalliomelane formed probably at conditions typical for MnO_2 precipitates with the highest Eh potential marked in the assemblage, reaching +0.5–0.6 V at the previously mentioned pH values (Fig. 5). Above the Eh, according to the stability diagram of I (Brookins 1988; Takeno 2005), iodides oxidize to iodates, which were not found at Zalas.

In a recent study on the sorption of Tl onto various Mn oxides (Wick et al. 2019), it has been shown that hexagonal vacancy-containing birnessite can sorb Tl by oxidation and complexation. In contrast, triclinic birnessite as well as todorokite were observed to sorb hydrated Tl^+ in their interlayers or tunnels without oxidation. Synthetic cryptomelane was found to sorb high levels of dehydrated Tl^+ by exchange of structural K; with the replacement of up to ~1/3 of the initial K. While this exchange process was not studied in detail with respect to cation exchange selectivity or limits of structural exchange, it is probable that the extent of Tl-for-K exchange depends on the dissolved concentrations of Tl^+ and K^+ as well as on structural factors, as reported for the uptake of Rb^+ and Cs^+ by cryptomelane (Tsuji and Komarneni 1993; Tsuji et al. 1993). Thus, we speculate that thalliomelane at Zalas could have formed from a cryptomelane-type precursor phase exposed to Tl-enriched fluids via gradual Tl-for-K exchange over extended periods of time. However, to constrain the potential pathways for thalliomelane formation, further insights into Tl-for-K exchange in cryptomelane and into the reactions of Tl with other Mn oxides are needed,

as well as further mineralogical observations on the occurrence of thalliomelane or other Tl-bearing Mn-oxides in natural settings.

ACKNOWLEDGMENTS AND FUNDING

We thank Sergey Krivovichev, an anonymous reviewer and the technical reviewer for their comments that were very helpful to improve the manuscript. We also thank Ralph Steininger (KIT, Germany) for his support during XAS data collection, and Sam Webb (Stanford Synchrotron Radiation Laboratory, Menlo Park, USA) and Alain Manceau (University of Grenoble, France) for sharing XAS reference spectra of Mn oxides. This study was financially supported by the AGH UST grant 16.16.140.315 to BG.

REFERENCES

Balić-Žunić, T., Moëlo, Y., Lončar, Ž. and Micheelsen, H. (1994) Dorallcharite, $Tl_{0,8}K_{0,2}Fe_3(SO_4)_2(OH)_6$, a new mineral of the jarosite–alunite family. European Journal of Mineralogy, 6, 255–263.

Biagioni, C., Capalbo, C. and Pasero, M. (2013) Nomenclature tunings in the hollandite supergroup. European Journal of Mineralogy, 25, 85–90.

Biagioni, C., Capalbo, C., Lezzerini, M. and Pasero, M. (2014) Ferrihollandite, $BaMn^{4+}_6Fe^{3+}_2O_{16}$, from Apuan Alps, Tuscany, Italy: description and crystal structure. European Journal of Mineralogy, 26, 171–178.

Bidoglio, G., Gibson, P.N., O'Gorman, M. and Roberts, K.J. (1993) X-ray absorption spectroscopy investigation of surface redox transformations of thallium and chromium on colloidal mineral oxides. Geochimica at Cosmochimica Acta, 57, 2389–2394.

Brookins, D.G. (1988) Eh-pH Diagrams for Geochemistry. Springer-Verlag Berlin.

Chukanov, N.V., Aksenov, S.M., Jančev, S., Pekov, I.V., Göttlicher, J., Polekhovsky, Yu.S., Rusakov, V.S., Nelyubina, Y.V. and Van, K.V. (2016) A new mineral species ferricoronadite, $Pb[Mn_6^{4+}(Fe^{3+},Mn^{3+})_2]O_{16}$: mineralogical characterization, crystal chemistry and physical properties. Physics and Chemistry of Minerals, 43, 503–514.

Critteden, M.S., Cuttitta, F., Rose, H.D. and Fleischer, M. (1962) Studies on manganese oxide minerals VI. Thallium in some manganese oxides. American Mineralogist, 47, 1461–1467.

Cruz-Hernández, Y., Villalobos, M., Marcus, M.A., Pi-Puig, T., Zanella, R., Martínez-Villegas, N. (2019) Tl(I) sorption behavior on birnessite and its implications for mineral structural changes. Geochimica et Cosmochimica Acta, 248, 356–369.

Cruz-Hernández, Y., Göttlicher, J., Pi-Puig, T., Ruiz-García, M., Villalobos, M. and Voegelin, A. (2020) Mechanisms of Tl(I) sorption and structural effects on poorly crystalline birnessites as a function of Tl(I) concentration. GEOC 6; American Chemical Society Fall 2020, Virtual Meeting and EXPO, August 17–20.

Daiyan, C., Guanxin, W., Zhenxi, Z. and Yuming, C. (2003) Lanmuchangite, a new thallium (hydrous) sulphate from Lanmuchang, Guizhou Province, China. Chinese Journal of Geochemistry, 22/2, 185–192.

Filatov, S.K., Vergasova, L.P., Siidra, O.I., Krivovichev, S.V. and Kretser, Y.L. (2013) Markhininite , IMA 2012-040. CNMNC Newsletter No. 15, February 2013, page 2; Mineralogical Magazine, 77, 1–12.

Gaines, R.V., Skinner, H.C., Foord, E.E., Mason, B. and Rosenzweig, A. (1997) Dana's New Mineralogy, Eighth Edition, John Wiley & Sons, Inc, New York.

Gjönnes, K. (1997) On the integration of electron diffraction intensities in the Vincent-Midgley precession technique. Ultramicroscopy, 69, 1–11.

383 Gołębiowska, B., Pieczka, A., Rzepa, G., Matyszkiewicz, J. and Krajewski, M. (2010)
384 Iodargyrite from Zalas (Cracow area, Poland) as an indicator of Oligocene–Miocene aridity in
385 Central Europe. Palaeogeography, Palaeoclimatology, Palaeoecology, 296, 130–137.
386 Gołębiowska, B., Rzepa, G. and Pieczka, A. (2015) Exceptional Tl-bearing manganese oxides
387 from Zalas, Kraków area, southern Poland. Mineralogia, 46, 3–17.
388 Gołębiowska, B., Pieczka, A., Zubko, M., Voegelin, A., Göttlicher, J. and Rzepa, G. (2019)
389 Thalliomelane, IMA 2019-055. CNMNC Newsletter No. 52; Mineralogical Magazine, 83,
390 888.
391 Haynes, B.W., Law, S.S., Barron, D.C., Kramer, G.W., Maeda, R. and Magyar, M.J. (1985)
392 Pacific manganese nodules: characterization and processing. Bulletin of the United States
393 Department of the Interior, Bureau of Mines, 679.
394 Hein, J.R., Conrad, T.A., Frank, M., Christl, M. and Sager, W.W. (2012) Copper-nickel-rich,
395 amalgamated ferromanganese crust-nodule deposits from Shatsky Rise, NW Pacific.
396 Geochemistry, Geophysics, Geosystems, 13, 1–23.
397 Hewett, D.F. (1968) Silver in veins of hypogene manganese oxides. Geological Survey Circular,
398 553, United States Department of the Interior. Washington.
399 Jezequel, P., Wille, G., Bény, C., Delorme, F., Jean-Prost, V., Cottier, R., Breton, J., Duré, F. and
400 Despriee, J. (2011) Characterization and origin of black and red Magdalenian pigments from
401 Grottes de la Garenne (Valléemoyenne de la Creuse-France): a mineralogical and geochemical
402 approach of the study of prehistorical paintings. Journal of Archaeological Science, 38, 1165–
403 1172.
404 Karpova, K.N., Kon'kova, E.A., Larkin, E.D. and Savel'ev, V.F. (1958) Avicennite, a new
405 mineral (in Russian). Doklady Akademii Nauk Uzbekistan SSR, 2, 23–26.

406 Kolb, U., Gorelik, T., Kübel, C., Otten, M.T. and Hubert, D. (2007) Towards automated
407 diffraction tomography: Part I—Data acquisition. Ultramicroscopy, 107, 507–513.
408 Koschinsky, A. and Hein, J.R. (2003) Uptake of elements from seawater by ferromanganese
409 crusts: solid phase associations and seawater speciation. Marine Geology, 198, 331–351.
410 Lin, T.S. and Nriagu, J. (1998) Revised hydrolysis constants for thallium(I) and thallium(III) and
411 the environmental implications. Journal of the Air & Waste Management Association, 48,
412 151–156.
413 Manceau, A., Kersten, M., Marcus, M.A., Geoffroy, N. and Granina, L. (2007) Ba and Ni
414 speciation in a nodule of binary Mn oxide phase composition from Lake Baikal. Geochimica
415 et Cosmochimica Acta, 71, 1967–1981.
416 Mandarino, J.A. (1979) The Gladstone-Dale relationship. Part III. Some general applications.
417 Canadian Mineralogist, 17, 71–76.
418 Mandarino, J.A. (1981) The Gladstone-Dale relationship. Part IV. The compatibility concept and
419 its application. Canadian Mineralogist, 19, 441–450.
420 Mathieson, A.M. and Wadsley, A.D. (1950) The crystal structure of cryptomelane. American
421 Mineralogist, 35, 99–101.
422 Meisser, N., Perseil, E.A., Brugger, J. and Chiappero, P.J. (1999) Strontiomelane,
423 $SrMn^{4+}_{6}Mn^{3+}_{2}O_{16}$, a new mineral species of the cryptomelane group from St. Marcel -
424 Praborna, Aosta Valley, Italy. Canadian Mineralogist, 37, 673–678.
425 Nambu, M. and Tanida, K. (1967) Manjiroite, a new manganese dioxide mineral, from Kohare
426 Mine, Iwate Prefecture, Japan. Journal of the Japanese Association of Mineralogists,
427 Petrologists and Economic Geologists, 58, 39–54 (in Japanese).
428 Nawrocki, J., Polechońska, O., Lewandowska, A. and Werner, T. (2005) On the palaeomagnetic
429 age of the Zalas laccolith (southern Poland). Acta Geologica Polonica, 55, 229–236.

Palatinus, L., Brázda, P., Jelínek, M., Hrdá, J., Steciuk, G. and Klementová, M. (2019) Specifics of the data processing of precession electron diffraction tomography data and their implementation in the program PETS2.0. Acta Crystallographica, B75, 512–522.

Peacock, C.L. and Moon, E.M. (2012) Oxidative scavenging of thallium by birnessite: explanation for thallium enrichment and stable isotope fractionation in marine ferromanganese precipitates. Geochimica et Cosmochimica Acta, 84, 297–313.

Pekov, I.V., Zubkova, N.V., Belakovskiy, D.I., Vigasina, M.F., Sidorov, E.G. and Pushcharovsky, D.Y. (2013) Chrysothallite, IMA 2013-008. CNMNC Newsletter No. 16, August 2013, page 2702. Mineralogical Magazine, 77, 2695–2709.

Pekov, I.V., Zubkova, N.V., Belakovskiy, D.I., Yapaskurt, V.O., Vigasina, M.F., Lykova, I.S., Sidorov, E.G., Pushcharovsky, D.Y. (2015) Chrysothallite $K_6Cu_6Tl^{3+}Cl_{17}(OH)_4 \cdot H_2O$, a new mineral species from the Tolbachik volcano, Kamchatka, Russia. Mineralogical Magazine, 79, 365–376.

Petříček, V., Dušek, M. and Palatinus, L. (2014) Crystallographic computing system JANA2006: General features. Zeitschrift für Kristallographie - Crystalline Materials, 229, 345–352.

Post, J.E. (1999) Manganese oxide minerals: Crystal structures and economic and environmental significance. Proceedings of the National Academy of Science of the United States of America, 96, 3447–3454.

Post, J.E. and Bish, D.L. (1989) Rietveld refinement of the coronadite structure. American Mineralogist, 74, 913–917.

Post, J.E., Von Dreele, R.B. and Buseck, P.R. (1982) Symmetry and cation displacements in hollandites: structure refinements of hollandite, cryptomelane and priderite. Acta Crystallographica, B38, 1056–1065.

453 Pouchou, J.-L. and Pichoir, F. (1991) Quantitative analysis of homogeneous or stratified
454 microvolumes applying the model "PAP". In Electron Probe Quantitation; Heinrich, K.F.J.,
455 Newbury, D.E., eds., Plenum Press: New York, NY, USA, 1991; pp. 3l–75.
456 Reich, M., Palacios, C., Alvear, M., Cameron, E.M., Leybourne, M.I. and Deditius, A. (2009)
457 Iodine-rich waters involved in supergene enrichment of the Mantos de la Luna argentiferous
458 copper deposit, Atacama Desert, Chile. Mineralium Deposita, 44, 719–722.
459 Rumsey, M.S., Mills, S.J., Spratt, J., Hay, D.G. and Farber, G. (2014) Thalliumpharmacosiderite,
460 IMA 2013-124. CNMNC Newsletter No. 20, June 2014, page 553; Mineralogical Magazine,
461 78, 549–558.
462 Savenko, V.S. (2000) Solubility of thallium(III) hydroxide in aqueous solution. Russian Journal
463 of Inorganic Chemistry, 45, 1619–1620.
464 Shannon, R.D. (1976) Revised effective ionic radii and systematic studies of interatomic
465 distances in halides and chalcogenides. Acta Crystallographica, A32, 751–767.
466 Sheldrick, G. M. (2015) Crystal structure refinement with *SHELXL*. Acta Crystallographica, C71,
467 3–8.
468 Siidra, O.I., Vergasova, L.P., Kretser, Y.L., Polekhovsky, Y.S., Krivovichev, S.V. and Filatov,
469 S.K. (2013) Evdokimovite, IMA 2013-041. CNMNC Newsletter No. 17, October 2013, page
470 2999; Mineralogical Magazine, 77, 2997–3005.
471 Siidra, O.I., Vergasova, L.P., Krivovichev, S.V., Kretser, Y.L., Zaitsev, A.N. and Filatov, S.K.
472 (2014a) Unique thallium mineralization in the fumaroles of Tolbachik volcano, Kamchatka
473 Peninsula, Russia. I. Markhininite, $TlBi(SO_4)_2$. Mineralogical Magazine, 78, 1687–1698.
474 Siidra, O.I., Vergasova, L.P., Kretser, Y.L., Polekhovsky, Y.S., Filatov, S.K. and Krivovichev,
475 S.V. (2014b) Unique thallium mineralization in the fumaroles of Tolbachik volcano,

476 Kamchatka Peninsula, Russia. II. Karpovite, $Tl_2VO(SO_4)_2(H_2O)$. Mineralogical Magazine 78,
477 1699–1709.
478 Siidra, O. I., Vergasova, L. P., Kretser, Y. L., Polekhovsky, Y. S., Filatov, S. K. and Krivovichev,
479 S.V. (2014c) Unique thallium mineralization in the fumaroles of Tolbachik volcano,
480 Kamchatka Peninsula, Russia. III. Evdokimovite, $Tl_4(VO)_3(SO_4)_5(H_2O)_5$. Mineralogical
481 Magazine, 78, 1711–1724.
482 Strunz, H. and Nickel, E.H. (2001) Strunz Mineralogical Tables, Ninth Edition.
483 Schweizerbart'sche Verlagsbuchhandlung, Stuttgart.
484 Takeno, N. (2005) Atlas of Eh-pH diagrams. Intercomparison of thermodynamic databases.
485 Geological Survey of Japan Open File Report No.419. National Institute of Advanced
486 Industrial Science and Technology; Research Center for Deep Geological Environments.
487 Tsuji, M. and Komarneni, S. (1993) Powder X-ray diffraction study of a cryptomelane-type
488 manganic acid and its alkali cation exchanged forms. Journal of Material Research, 8, 3145–
489 3150.
490 Tsuji, M., Komarneni, S. and Abe, M. (1993) Ion-exchange selectivity for alkali metal ions on a
491 cryptomelane-type hydrous manganese dioxide. Solvent Extraction and Ion Exchange, 11,
492 143–158.
493 Vergasova, L.P., Siidra, O.I., Kretser, Y.L., Polekhovsky, Y.S., Filatov, S.K. and Krivovichev,
494 S.V. (2013) Karpovite, IMA 2013-040. CNMNC Newsletter No. 17, October 2013, page
495 2999; Mineralogical Magazine, 77, 2997–3005.
496 Vincent, R. and Midgley, P.A. (1994) Double conical beam-rocking system for measurement of
497 integrated electron diffraction intensities. Ultramicroscopy, 53, 271–282.
498 Vink, B.W. (1993) The behaviour of thallium in the (sub)surface environment in terms of Eh and
499 pH. Chemical Geology, 109, 119–123.

Voegelin, A., Pfenninger, N., Petrikis, J., Majzlan, J., Plötze, M. and Senn, A. C. (2015) Thallium speciation and extractability in a thallium- and arsenic-rich soil developed from mineralized carbonate rock. Environmental Science Technology, 49, 5390–5398.

Voskresenskaya, N.T. and Soboleva, L.T. (1961) Once more on thallium in manganese minerals (in Russian with English summary). Geokhimiya, 3, 276–278.

Webb, S.M., Tebo, B.M. and Bargar, J.R. (2005) Structural characterization of biogenic Mn oxides produced in seawater by the marine bacillus sp. strain SG-1. American Mineralogist, 90, 1342–1357.

Wick, S., Baeyens, B., Marques Fernandes, M. and Voegelin, A. (2018) Thallium adsorption onto illite. Environmental Science & Technology, 52, 571–580.

Wick, S., Peña, J. and Voegelin, A. (2019) Thallium sorption onto manganese oxides. Environmental Science & Technology, 53, 13168–13178.

512 **Figure captions:**

513 **Figure 1**. Thalliomelane aggregates in Jurassic sandy limestone from Zalas. Scale bar – 10 μm.

514 **Figure 2**. Micro-XRF element distribution maps around a selected (Tl,Mn)-rich particle
515 (thalliomelane) in $CaCO_3$ matrix (~25-μm beam, step size 10 μm). Scale bar – 500 μm.

516 **Figure 3**. (a) Tl L_{III}-edge XANES spectrum of thalliomelane particle, the same as referred in Fig.
517 2 (black lines) compared to reference spectra for Tl^{3+} [Tl_2O_3, blue line, from Voegelin et al.
518 (2015) and Tl^+ (aqueous Tl^+, red line, from Wick et al. (2018)]; (b) Mn *K*-edge EXAFS spectrum
519 of thalliomelane particle (black lines) compared to reference spectra of triclinic birnessite (green
520 line), todorokite (red line) and hollandite (blue line). The reference spectra for triclinic birnessite
521 and todorokite from Webb et al. (2005) were kindly provided by Sam Webb (Stanford
522 Synchrotron Radiation Laboratory, Menlo Park, USA); the reference spectrum for hollandite
523 from Manceau et al. (2007) was kindly provided by Alain Manceau (University of Grenoble,
524 France).

525 **Figure 4**. View of the crystal unit cell of thalliomelane along: (a) [100] direction, (b) [001]
526 direction, (c) arbitrary direction, (d) [001] direction showing the channels in the structure.
527 Symbols: (Mn^{4+},Cu^{2+}) octahedra are presented in violet color; red spheres – oxygen atoms; grey
528 ellipses – possible Tl positions.

529 **Figure 5**. The pH-Eh diagram for the primary and supergene minerals at Zalas. Data for Cu and
530 Ag minerals and dissolved species of Cu, Ag, S, Cl, CO_2 and I are taken from Reich et al. (2009),
531 data for Mn oxides and dissolved Mn species from Takeno (2005), Tl is not shown because at
532 Zalas it precipitated along with MnO_2 as Tl^+, which corresponds to the stable Tl oxidation state
533 over the pH–Eh range of H_2O. Grey arrow marks a supposed pH–Eh evolution path of the
534 assemblage; greenish field corresponds to conditions under which thalliomelane could form,

535 however due to direction of the changes in the pH–Eh space the most probable conditions

536 correspond to pH ~9–10 and Eh ~0.4–0.5 V. Abbreviations: Haus – hausmannite.

Table 1. Chemical composition of thalliomelane.

component	mean (wt%)	range (wt%)	sd (wt%)	ion	apfu	sd (apfu)
SiO_2	0.17	0.08 – 0.57	0.14	Si^{4+}	0.025	0.021
MnO_2	67.23	65.02 – 68.85	0.89	Mn^{4+}	7.154	0.115
Al_2O_3	0.02	b.d.l. – 0.06	0.02	Al^{3+}	0.004	0.004
Fe_2O_3	0.49	0.24. – 1.14	0.25	Fe^{3+}	0.057	0.028
CoO	0.64	0.28. – 1.16	0.32	Co^{2+}	0.079	0.034
NiO	0.23	0.15. – 0.30	0.06	Ni^{2+}	0.028	0.006
MgO	0.05	b.d.l. – 0.12	0.04	Mg^{2+}	0.012	0.009
CuO	5.47	4.83 – 6.21	0.47	Cu^{2+}	0.636	0.044
ZnO	0.04	b.d.l. – 0.15	0.04	Zn^{2+}	0.004	0.005
SrO	0.01	b.d.l. – 0.06	0.03	Sr^{2+}	0.001	0.002
BaO	3.53	2.89 – 4.39	0.56	Ba^{2+}	0.213	0.032
PbO	0.14	0.06 – 0.20	0.05	Pb^{2+}	0.006	0.002
Na_2O	0.04	b.d.l. – 0.06	0.01	Na^{+}	0.011	0.004
K_2O	0.14	0.08 – 0.20	0.04	K^{+}	0.027	0.007
Tl_2O	17.67	15.18 – 20.83	2.09	Tl^{+}	0.770	0.105
$H_2O_{calc.}$	0.32	0.00 – 0.70	0.24	OH^{-}	0.332	0.236
				O^{2-}	15.668	0.236
Total	96.19 [1)]					

Normalization of the analysis is made on the basis of 16 (O, OH) anions and 8 cations per formula unit; $H_2O_{calc.}$ – calculated by charge balance; [1)] mean analysis of thalliomelane is completed by an admixture of the host limestone (1.82 wt% CaO determined with EPMA and 1.43 wt% CO_2 calculated on the basis of calcite stoichiometry), which give the mean sum of components in the analyzed spots equal to 99.42 wt% (see explanations in the text).

Table 2. TEM diffraction data (d in Å) for thalliomelane (only reflections with $I > 1$ are presented).

I_{meas}	d_{calc}	hkl	I_{meas}	d_{calc}	hkl
19	4.9332	0 2 0	8	1.2410	0 4 2
85	**3.1200**	**1 3 0**	10	1.2333	0 8 0
5	2.7576	0 1 1	4	1.2257	-2 7 1
39	**2.4666**	**0 4 0**	2	1.2257	2 7 1
66	**2.4071**	**1 2 1**	2	1.2219	3 3 2
10	2.4071	-1 2 1	8	1.2035	2 4 2
23	2.2062	2 4 0	9	1.1965	2 8 0
66	**2.1633**	**0 3 1**	3	1.1965	-2 8 0
25	1.9350	-1 5 0	8	1.1532	-1 5 2
14	1.9350	1 5 0	6	1.1532	1 5 2
45	**1.8385**	**-1 4 1**	5	1.1470	5 7 0
18	1.8385	1 4 1	3	1.1258	1 8 1
5	1.6921	3 5 0	2	1.1258	-1 8 1
100	**1.6444**	**0 6 0**	2	1.1031	4 8 0
4	1.6264	0 5 1	1	1.0949	3 5 2
21	1.5600	2 6 0	14	1.0896	1 9 0
39	1.5446	2 5 1	4	1.0896	-1 9 0
76	**1.4361**	**0 0 2**	24	1.0817	0 6 2
10	1.4124	-1 6 1	3	1.0715	3 8 1
4	1.4124	1 6 1	5	1.0400	3 9 0
6	1.4066	1 1 2	3	1.0242	0 9 1
11	1.3953	1 7 0	6	1.0028	-2 91
1	1.3953	-1 7 0	2	1.0028	6 7 1
9	1.3788	0 2 2	1	1.0028	2 9 1
2	1.3682	4 6 0	5	1.0073	1 7 2
12	1.3578	4 5 1	2	0.9906	4 6 2
3	1.3279	2 2 2	13	0.9866	0 10 0
3	1.3091	3 6 1	1	0.9827	5 8 1
10	1.3045	1 3 2	7	0.9675	-2 10 0
4	1.3045	-1 3 2	1	0.9675	2 10 0
10	1.2955	3 7 0	5	0.9619	3 7 2
2	1.2653	0 7 1			

Table 3. Comparative compositional and structural data for minerals of the coronadite group.

	Coronadite	Ferricoronadite	Hollandite	Ferriholandite	Cryptomelane	Manjiroite	Strontiomelane	Thalliomelane
Formula	$Pb(Mn^{4+}_{6}Mn^{3+}_{2})O_{16}$	$Pb(Mn^{4+}_{6}Fe^{3+}_{2})O_{16}$	$Ba(Mn^{4+}_{6}Mn^{3+}_{2})O_{16}$	$Ba(Mn^{4+}_{6}Fe^{3+}_{2})O_{16}$	$K(Mn^{4+}_{7}Mn^{3+})O_{16}$	$Na(Mn^{4+}_{7}Mn^{3+})O_{16}$	$Sr(Mn^{4+}_{6}Mn^{3+}_{2})O_{16}$	$TlMn^{4+}_{7.5}Cu^{2+}_{0.5}O_{16}$
crystal system	monoclinic	tetragonal	monoclinic	monoclinic	monoclinic	tetragonal	monoclinic	tetragonal
space group	*I*2/*m*	*I*4/*m*	*I*2/*m*	*I*2/*m*	*I*2/*m*	*I*4/*m*	*I*2/*m*	*I*4/*m*
a (Å)	9.938(2)	9.9043(7)	10.026	10.0001(7)	9.956	9.916	10.00(1)	9.8664(12)
b (Å)	2.8678(5)	9.9043(7)	2.878	5.7465(4)	2.8705	9.916	5.758(7)	9.8664(12)
c (Å)	9.834(2)	2.8986(9)	9.729	9.8076(8)	9.706	2.864	9.881(1)	2.8721(4)
β (º)	90.39(2)	90	91.03	90.713(2)	90.95	90	90.64(6)	90
V ($Å^3$)	280.26	284.34(9)	279.48	563.36	277.35	281.61	568.85	279.59(8)
Z	1	1	1	2	1	1	2	1
a:*b*:*c*	3.465:1:3.429	1:1:0.293	3.484:1:3.380	1.740:1:1.707	3.468:1:3.381	1:1:0.289	1.737:1:1.716	1:1:0.291
Reference	Post and Bish (1989)	Chukanov et al. (2016)	Post et al. (1982)	Biagioni et al. (2014)	Mathieson and Wadsley (1950)	Nambu and Tanida (1967)	Meisser et al. (1999)	this study

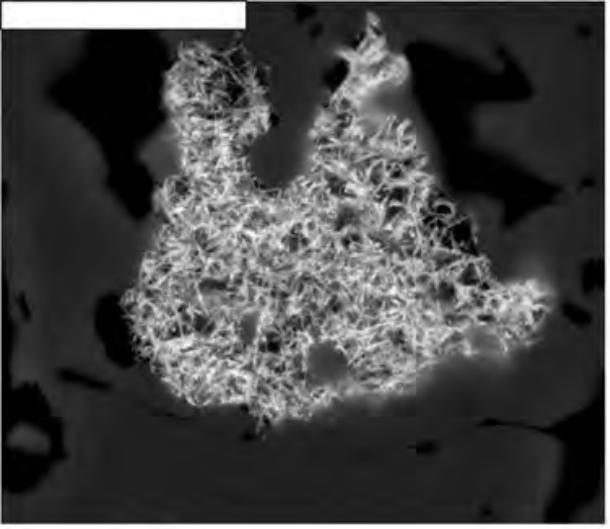

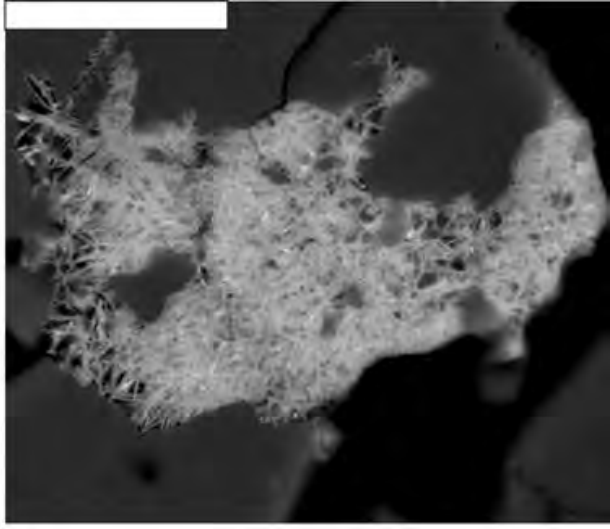

Fig. 1.

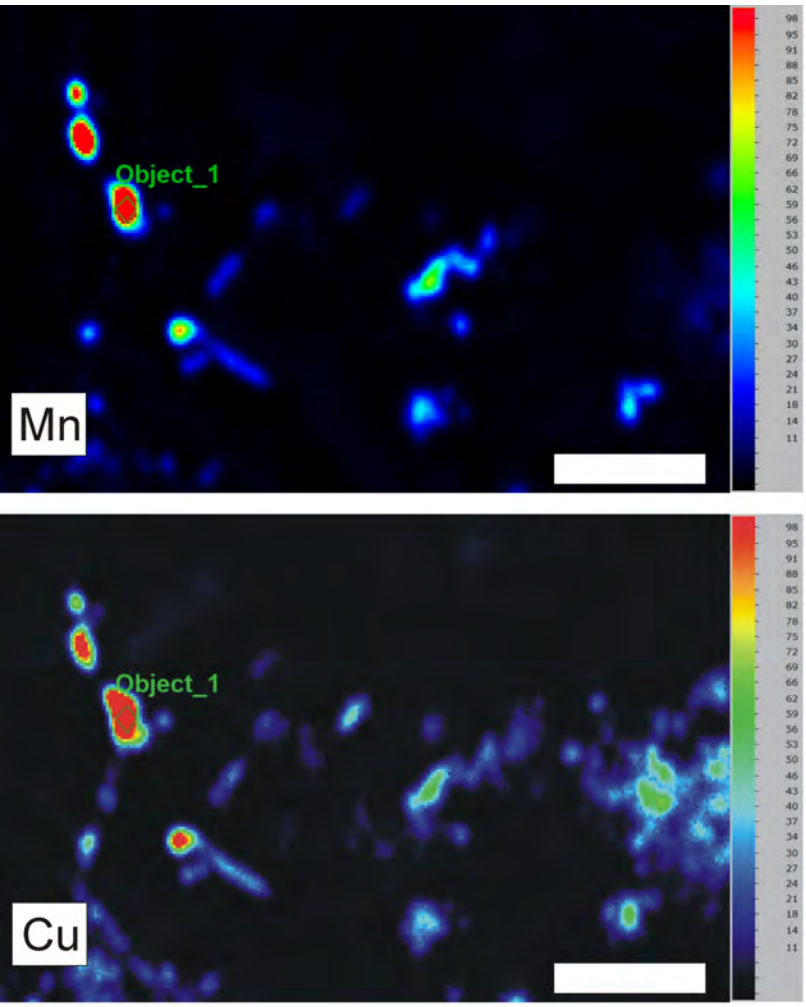

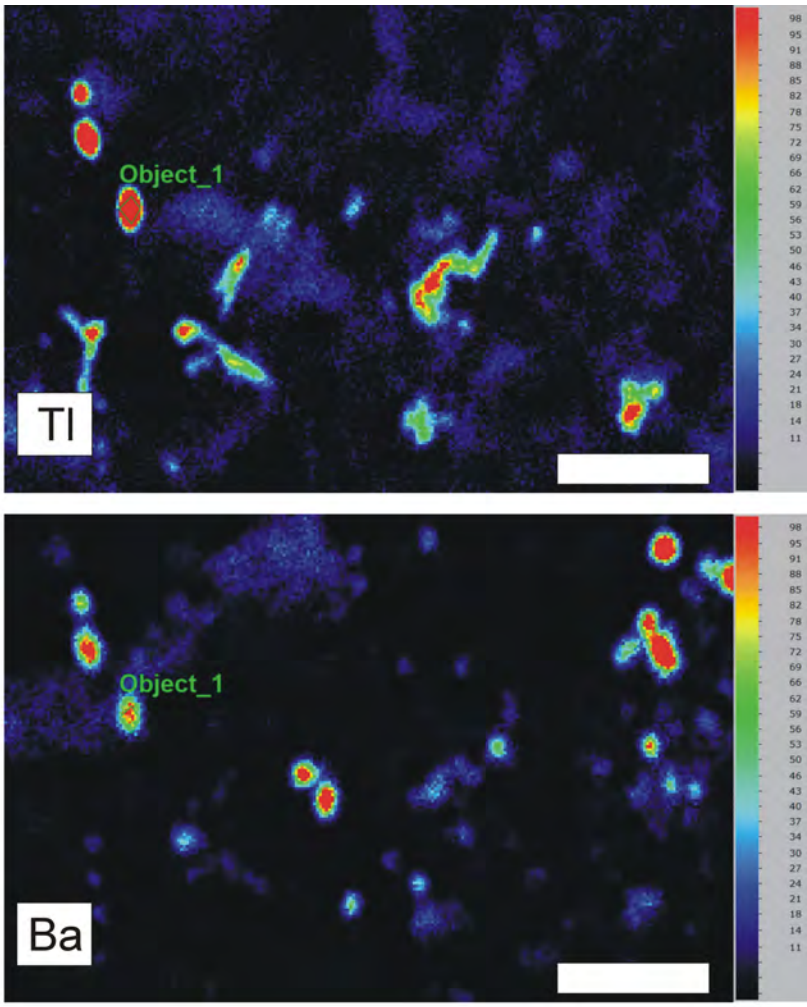

Fig. 2.

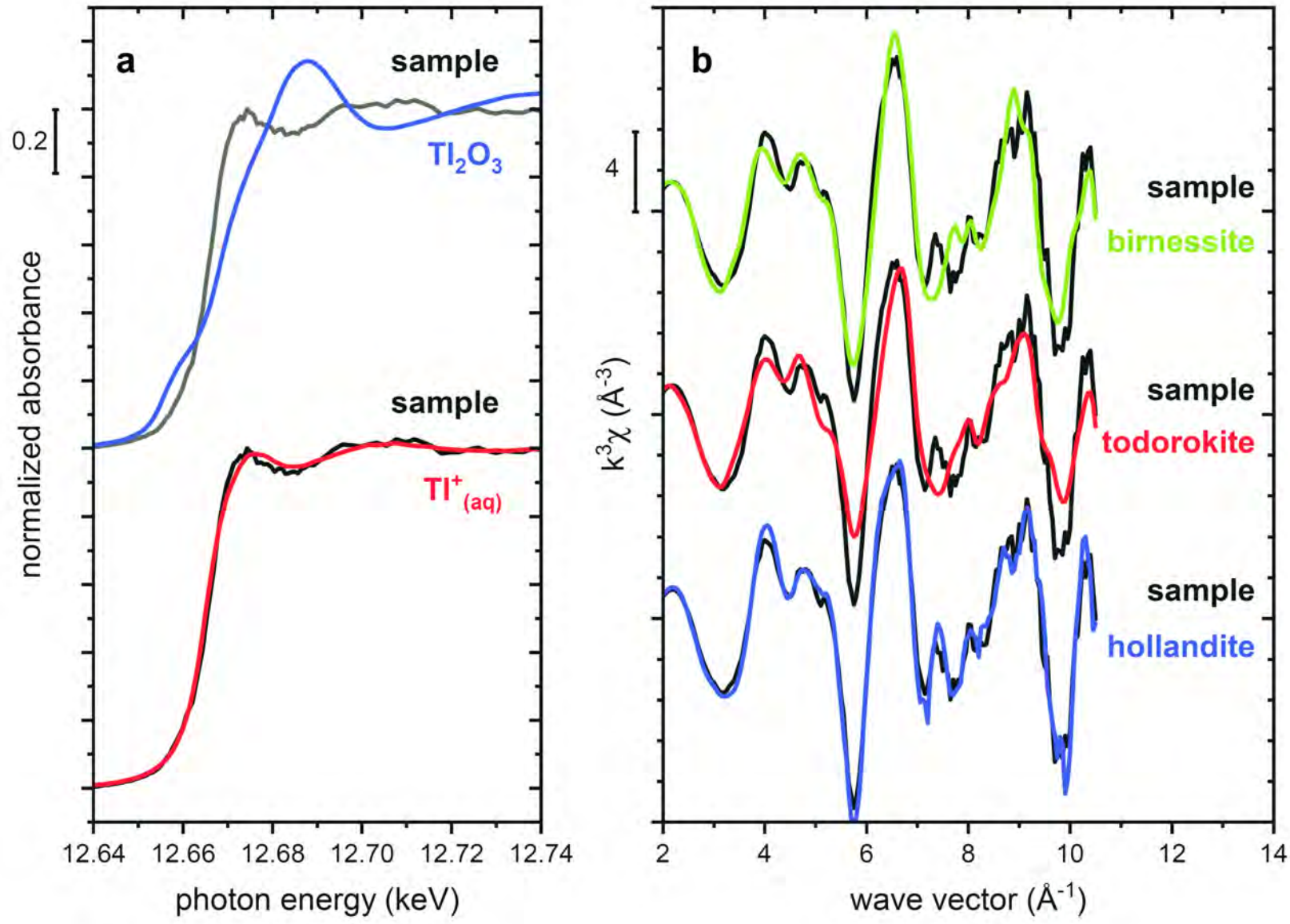
a
sample
Tl_2O_3
sample
$Tl^+_{(aq)}$
0.2
normalized absorbance
12.64
12.66
12.68
12.70
12.72
12.74
photon energy (keV)
b
4
$k^3\chi$ (Å^{-3})
sample
birnessite
sample
todorokite
sample
hollandite
2
4
6
8
10
12
14
wave vector (Å^{-1})

Fig. 3.

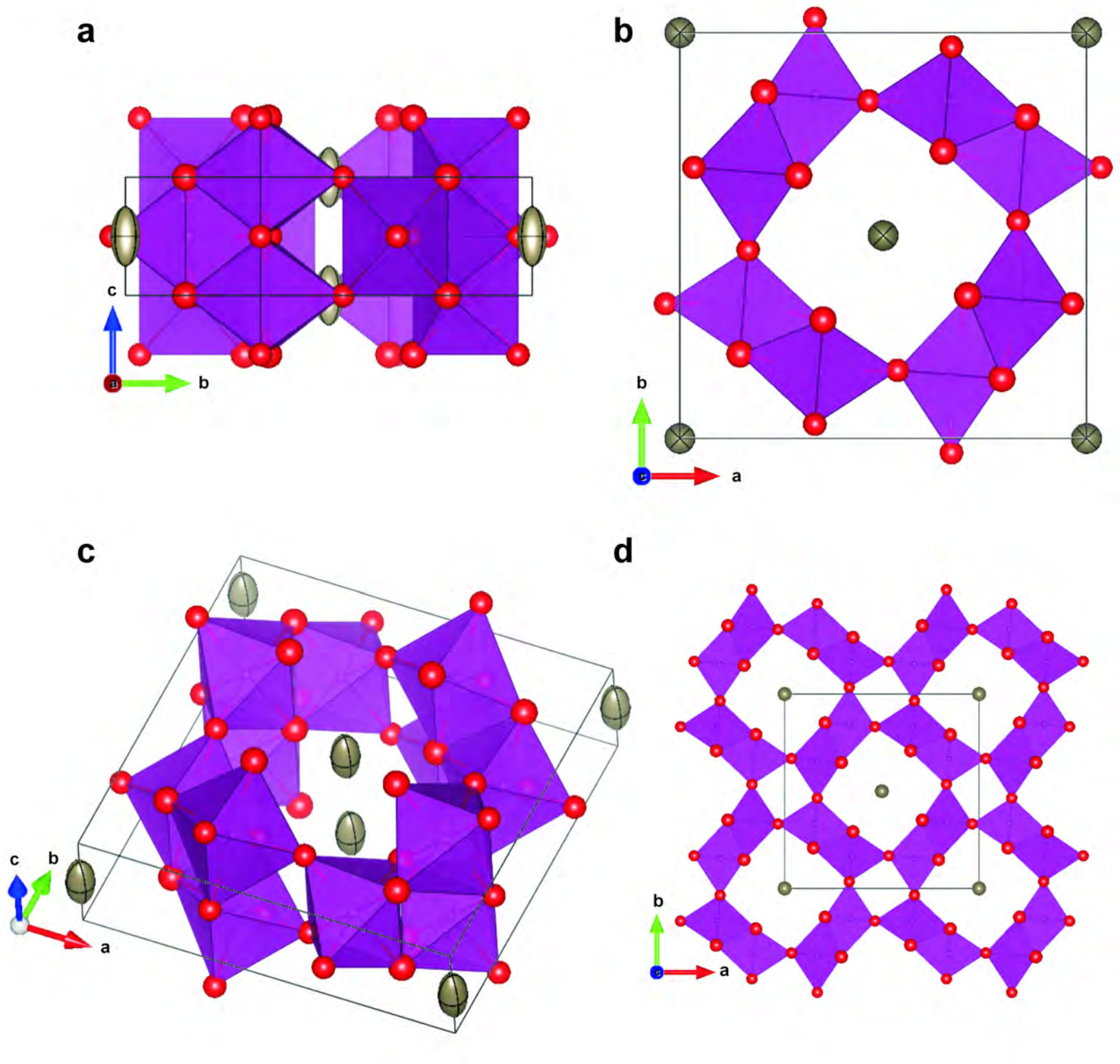

Fig. 4.

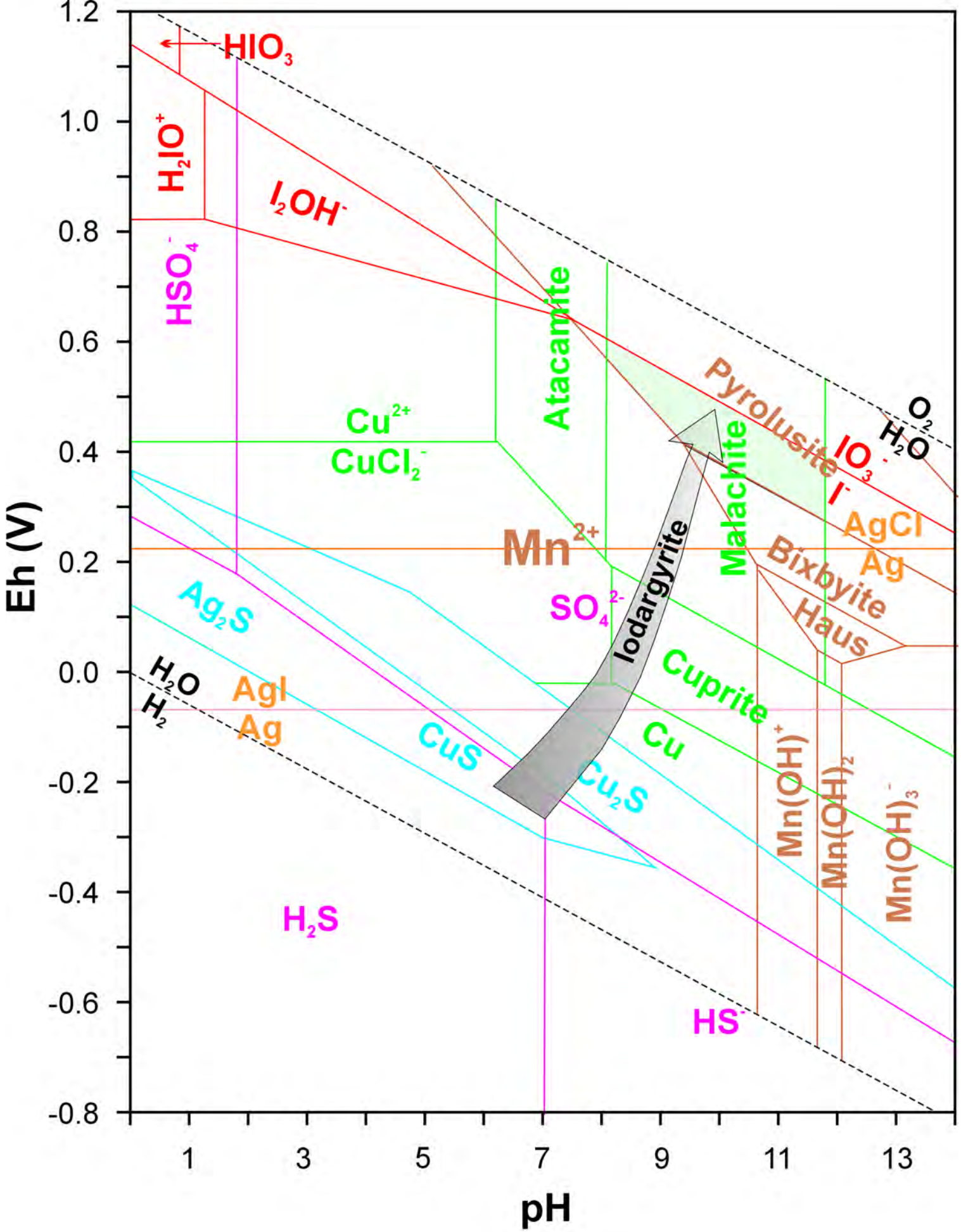
HIO3
H2IO+
I2OH-
HSO4-
Cu2+
CuCl2-
Atacamite
Pyrolusite
IO3-
I-
O2
H2O
AgCl
Ag
Bixbyite
Haus
Malachite
Mn2+
SO42-
Iodargyrite
Ag2S
H2O
H2
AgI
Ag
CuS
Cu2S
Cuprite
Cu
Mn(OH)+
Mn(OH)2
Mn(OH)3-
H2S
HS-
Eh (V)
pH
1.2
1.0
0.8
0.6
0.4
0.2
0.0
-0.2
-0.4
-0.6
-0.8
1
3
5
7
9
11
13

Fig. 5.